Agricultural and Forest Meteorology

(This is a sample cover image for this issue. The actual cover is not yet available at this time.)
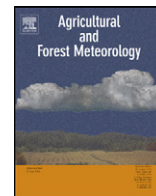
Spatial-scale effect on the SEBAL model for evapotranspiration estimation using remote sensing data

Ronglin Tang [a,b], Zhao-Liang Li [c,d,*], Kun-Shan Chen [b], Yuanyuan Jia [e], Chuanrong Li [e], Xiaomin Sun [f]

[a] State Key Laboratory of Resources and Environment Information System, Institute of Geographic Sciences and Natural Resources Research, Beijing 100101, China
[b] Center for Space and Remote Sensing Research, National Central University, Chung-Li, Taoyuan 320, Taiwan
[c] Key Laboratory of Agri-informatics, Ministry of Agriculture/Institute of Agricultural Resources and Regional Planning, Chinese Academy of Agricultural Sciences, Beijing 100081, China
[d] ICube, UdS, CNRS, Bld Sebastien Brant, BP10413, 67412 Illkirch, France
[e] Academy of Opto-Electronics, Chinese Academy of Sciences, Beijing 100190, China
[f] Key Laboratory of Ecosystem Network Observation and Modeling, Institute of Geographic Sciences and Natural Resources Research, Beijing 100101, China

A R T I C L E   I N F O

A B S T R A C T

The Surface Energy Balance Algorithm for Land (SEBAL) has been successfully applied to remote sensing data to estimate surface evapotranspiration (ET) at different spatial and temporal resolutions in more than 30 countries. However, the selection of dry and wet pixels over the area of interest (AOI) makes the SEBAL-estimated ET subject to the sizes of the AOI and the satellite pixels. This paper investigates the effect of the sizes of the AOI and satellite pixels on SEBAL-derived surface energy components by proposing generalized analytical equations. These equations demonstrate how the variations in the intermediate variables, the AOI, and the pixel size affect the resulting surface energy components and under which circumstances the sensible heat flux will be misestimated, without needing to run the SEBAL model. These analytical equations were verified through application to 23 clear-sky MODIS overpasses that cover different soil water contents and crop growth stages from January 2010 to late October 2011. The spatial effects of increasing the size of the AOI for SEBAL can be summarized as follows: (1) if the locations of dry and wet pixels do not vary, the pixel-by-pixel sensible heat flux (H_{LA}) calculated using the larger AOI is equal to that of the smaller AOI (H_{SA}, with $H_{LA}/H_{SA} = 1$), (2) if only the surface temperatures of wet pixels do not vary, the relative variation in H is equal to the relative variation of the slope (a) of the linear equation between the near-surface air temperature difference and the surface temperature ($H_{LA}/H_{SA} = 1 + \delta H_{SA}/H_{SA} = 1 + \delta a/a$), and (3) under other circumstances, H_{LA}/H_{SA} decreases with surface temperatures at a slowing pace from $\sim\infty$ at the temperature of the wet pixel ($T_{s,wet}$) to a certain value at the temperature of the dry pixel ($T_{s,dry}$) (both temperatures are for the small AOI). Analogously, a general analytical equation—a function of the coefficients of the linear equation between the near-surface air temperature difference and surface temperature at the high-resolution, the effective temperature, and the effective momentum roughness length—could be used to quantify the spatial-scale effect of the satellite pixel size. The findings from this study may help determine suitable sizes of the AOIs and the satellite pixels and aid in quantifying uncertainties in the SEBAL-derived surface energy components.

© 2013 Elsevier B.V. All rights reserved.

1. Introduction

Land surface evapotranspiration (ET) consumes 60% of the annual land precipitation in the global hydrological cycle (Oki and Kanae, 2006). Quantifying the distribution of the land surface ET at different temporal and spatial scales is critical to meteorology, hydrology, global climate change, and almost all other water-related scientific fields. There are more than 140 sites on five continents in the Fluxnet network that currently measure the exchanges of energy, water, and carbon dioxide between the land surface and the atmosphere (Baldocchi et al., 2001). However, these sparsely distributed tower sites are insufficient for local, regional, and global ET studies due to the heterogeneity of the earth's surface. Remote sensing provides a potential method to estimate ET at various scales.

* Corresponding author at: Key Laboratory of Agri-informatics, Ministry of Agriculture/Institute of Agricultural Resources and Regional Planning, Chinese Academy of Agricultural Sciences, Beijing 100081, China. Tel.: +86 1082105077.
E-mail addresses: lizl@unistra.fr, lizl@igsnrr.ac.cn, lizhaoliang@caas.cn (Z.-L. Li).

Over the past two decades, various remote sensing-based ET models, roughly classified as the end-member-based single-source models and the soil and vegetation energy/temperature separation two-source models, have been developed. These models include the Surface Energy Balance Algorithm for Land (Bastiaanssen, 1995; Bastiaanssen et al., 1998), surface temperature versus vegetation index triangle/trapezoid space (Price, 1990; Moran et al., 1994; Jiang and Islam, 1999; Tang et al., 2010), Simplified Surface Energy Balance Index (Roerink et al., 2000), Surface Energy Balance System (Su, 2002), Mapping Evapotranspiration with Internalized Calibration (Allen et al., 2007), the two-source N95 model (Norman et al., 1995), and the Atmosphere-Land Exchange Inverse model (Anderson et al., 1997). Li et al. (2009), among others, provides an overview of the limitations, advantages, and uncertainties of these commonly used ET models. The Surface Energy Balance Algorithm for Land (SEBAL), proposed by Bastiaanssen (1995) and Bastiaanssen et al. (1998), assumes a linear relationship between near-surface air temperature difference and surface temperature. It has been used to estimate the surface sensible heat flux and latent heat flux at different spatial and temporal resolutions in more than 30 countries (Bastiaanssen et al., 2005; Timmermans et al., 2007; Singh et al., 2008; Teixeira et al., 2009). Typical accuracies of the estimated ET in the SEBAL model are 85%, 95%, and 96% at daily, seasonal, and annual scales, respectively. The SEBAL model has several advantages over other approaches in estimating surface-energy fluxes from remote sensing data, including: (1) it uses minimal ground-based data, (2) the near-surface air temperature is not mandatory, unlike in many other bulk transfer models, and (3) a self-calibration process is automated in each region of interest through the identification of dry and wet pixels and the determination of the near-surface air temperature difference. The most current version of the SEBAL model (SEBAL2008) has incorporated three major refinements: (1) the effect of the land-surface slope and aspect in mountainous areas, (2) a correction of the advection effect, and (3) improved estimates of surface albedo and soil heat flux (Bastiaanssen et al., 2010).

A basic premise associated with the SEBAL model, in general, is that under the given atmospheric conditions, the area of interest exhibits an extreme contrast in surface hydrological condition so that the dry and wet pixels where sensible heat flux (H_{dry} and H_{wet}) and latent heat flux (LE_{dry} and LE_{wet}) are known a priori could coexist. Bastiaanssen et al. (2005) have suggested that the wet pixel can be identified in open water bodies or in well-irrigated agricultural fields whereas the dry bare soil surface may be a good candidate for the dry pixel when no other knowledge can be used for calibration. After determining the locations of the dry and wet pixels, a linear relationship between the near-surface air temperature difference (dT_s) and surface radiometric temperature (T_s) constructed by fitting data to the dry and wet pixels is further applied to estimate the pixel-by-pixel dT_s under intermediate hydrologic/surface temperature conditions (Fig. 1).

When SEBAL and other end-member-based models are used to estimate surface energy components, a concern is how large the area of interest (AOI) should be. A lack of general agreement on this issue brings about some uncertainties when the size of the AOI is varied, as the slope and intercept of the linear line between dT_s and T_s may have changed. To the best of our knowledge, there have been few studies dedicated to the effect of the size of the AOI on the sensible heat flux and latent heat flux derived using the SEBAL. Long et al. (2011) noted this heat flux difference by comparing the pixel-by-pixel sensible heat fluxes calculated for three different-sized sub-watersheds within the Baiyangdian watersheds in North China, and they concluded that the discrepancies in the sensible heat fluxes using the SEBAL are systematic for given atmospheric conditions when the AOI is expanded. However, it is unclear under which circumstances and how the sensible heat flux will change.

Determining the mechanism of this change in the SEBAL-derived surface energy fluxes is important for understanding the uncertainties that result from the selection of dry and wet pixels for given atmospheric conditions within a given AOI.

For a given AOI, the SEBAL model is also affected by the pixel size of the satellite data. In most cases, extremely dry or wet pixels may not exist in the low-resolution satellite view of the area of interest due to areas that contain both soil and vegetation. Compared with the low-resolution data, high-resolution satellite data are better able to capture the spatial variability of the surface, and therefore, the extremely dry and wet pixels are more readily identified. The SEBAL-derived surface energy components (surface net radiation, soil heat flux, sensible heat flux, and latent heat flux) may differ over an area when the satellite surface temperature at one scale is changed to a different scale. In previous studies (Long et al., 2011; Gebremichael et al., 2010; Hong et al., 2009; Compaoré et al., 2008), the uncertainty that results from the variation of pixel size in the SEBAL has generally been evaluated by comparing the ET estimated at a targeted lower resolution (e.g., MODIS) and the spatially averaged value derived by aggregating either output (output up-scaling) or input (input up-scaling) of the SEBAL with high-resolution data (e.g., TM/ETM+ or ASTER). Long et al. (2011), among others, have demonstrated the significant differences of the SEBAL-estimated sensible heat flux and latent heat flux using satellite data with different pixel sizes. They attributed the heat flux discrepancy to the difference in the range and magnitude of surface temperatures acquired at the different spatial resolutions. When the satellite pixel size is changed, estimates of the sensible heat flux and latent heat flux are influenced by a number of other factors, including variations in surface albedo, emissivity, and aerodynamic resistance (surface roughness length), in addition to the variation in surface temperature. Those inconclusive evaluations are far from an all-around apprehension of the mechanism implicit in the scaling transfer of the sensible and latent heat fluxes when the satellite pixel is coarsened.

The objective of this paper is to comprehensively quantify the spatial-scale effect of the SEBAL model caused by variation in the sizes of the AOI and satellite pixel on estimating the regional sensible heat flux and latent heat flux by proposing generalized analytical equations and through model application. We examine under which circumstances the sensible heat flux is overestimated/underestimated/unaltered in the SEBAL model when the size of the AOI is increased. We also investigate how the sensible and latent heat fluxes vary when high-spatial-resolution satellite data are aggregated with or replaced by low-resolution data. This study differs from previous studies primarily in two aspects: (1) the data cover a broad range of vegetation growth stages under a full range of vegetation cover and soil wetness conditions from January 2010 to late October 2011, allowing the inclusion of a variety of meteorological, surface vegetation, and soil moisture conditions; and (2) analytical equations are proposed to reveal the mechanism of the scaling transfer of the SEBAL model, which is different from previous studies that evaluate the spatial-scale effect of the SEBAL model by simple comparison and make inconsistent conclusions that depend on the meteorological, soil, and vegetation conditions. Moreover, these equations can help understand how uncertainties in the intermediate variables in the SEBAL model propagate to the resulting surface energy components due to the alteration of dry and wet pixels when the size of the AOI is changed or when using satellite data with different spatial resolutions. Section 2 presents the study area used as the AOI, the MODIS dataset, the SEBAL model theory, the spatial scaling theory, and how the simulations are carried out. In Section 3, the spatial-scale effect of the AOI size and satellite pixel size on the SEBAL model are presented and the proposed analytical equations are verified by comparing the pixel-by-pixel sensible (latent) heat flux with that estimated by directly
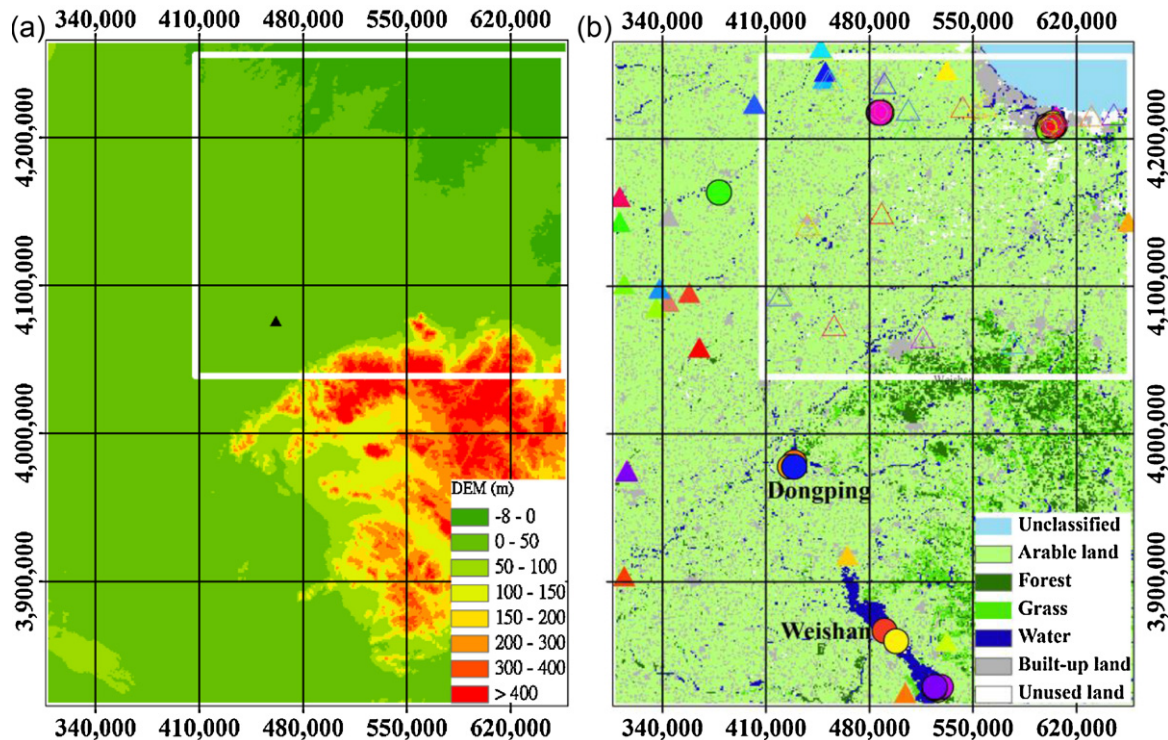
Fig. 1. (a) Digital elevation model at 1 km resolution in the UTM projection (zone number 50N) for the study area (http://eros.usgs.gov/#Find_Data/Products _and_Data_Available/gtopo30_info) with the location of the Yucheng station indicated by the black solid triangle, (b) a land-use map from 2005 with dry and wet pixels determined for the entire area and in the small AOI (the white rectangle in both figures). The solid triangles and circles with different colors indicate the dry and wet pixels, respectively, determined for the large AOI, and the hollow triangles and circles indicate the dry and wet pixels, respectively, determined for the small AOI at the 23 clear-sky MODIS overpass times from January 2010 to late October 2011. (For interpretation of the references to color in this figure legend, the reader is referred to the web version of the article.)

implementing the SEBAL model. Section 4 summarizes how the spatial-scale effect affects the SEBAL model.

2. Materials and methods

2.1. Study area

The study area (Fig. 1, hereafter referred to the large AOI) is part of the North China Plain. It is located from 34.5°N to 38.5°N and 114.8°E to 118.8°E and covers approximately 155,650 km^2 (349 samples × 446 lines at 1 km spatial resolution). The climate is humid and sub-humid in the warm temperate zone, and the soil is brunisolic. The surface elevation (Fig. 1a) varies primarily from 0 to 400 m above sea level. The land cover types are mainly arable (wheat, corn, cotton, sorghum, peanut), forest, grassland, water body (lake, river), and built-up land (Fig. 1b). Weishan Lake and Dongping Lake (Fig. 1b) are large lakes in the south and south-central portions of the study area. A small area (250 samples × 218 lines at 1 km spatial resolution, see the white rectangle in Fig. 1a and b) located in the northeast of the large AOI is used as the small AOI for evaluating the spatial domain effect on the SEBAL model. The Yucheng Comprehensive Experimental Station (36.8291°N/116.5703°E, hereafter referred to as the Yucheng station and identified by the solid black triangle in the middle of the large AOI in Fig. 1a) measures the downward and upward shortwave and longwave radiations with CNR-1 (Kipp & Zonen) radiometers and soil heat flux with a single HFP-01 soil heat flux plate (HukseFlux) at a soil depth of 2 cm. Winter wheat and summer corn are rotated as the main land covers at the Yucheng station. The annual temperature and precipitation are approximately 13.1 °C and 528 mm, respectively. Measurements of 10- and 30-min surface albedo (the ratio of upward to downward

shortwave radiations) and soil heat flux from January 2010 to late October 2011 at the Yucheng station cover different soil moisture conditions and crop growth stages and are used to calibrate the SEBAL model (see Section 2.3.2). For more detailed information on the Yucheng station, please refer to Tang et al. (2011).

2.2. Remote sensing data

The remote sensing data used in this study are from MODIS/ Terra and MODIS/Aqua products. The Terra and Aqua satellites, launched in December 1999 and May 2002, respectively, view the entire earth's surface every 1–2 days. The MODIS sensors onboard the Terra and Aqua satellites acquire data in 36 discrete spectral channels with a spatial resolution of 250 m for visible bands, 500 m for near-infrared bands, and 1000 m for the remaining thermal infrared bands. The data used in this study are retrieved from the Land Processes Distributed Active Archive Center (LP DAAC) and include land surface temperature/emissivity (MOD11_L2, MYD11_L2) at 1000 m spatial resolution and surface reflectance (MOD09GA, MYD09GA) at 500 m spatial resolution.

As the application of the SEBAL model requires an extreme surface hydrological contrast to ensure that dry and wet pixels exist, there should be as many valid pixels as possible within both the large and small AOIs. The MODIS/Terra and MODIS/Aqua overpasses are rigorously selected by adhering to the following rules:

(i) the maximum sensor-view zenith angle within the large AOI must be smaller than 45° to minimize the angular effect on the surface temperature (Li et al., 2001, 2004, 2013), and

(ii) pixels with valid temperature data should account for at least 80% of the total area in both the large and small AOIs.

Table 1
23 MODIS/Terra and MODIS/Aqua clear-sky overpasses used in this study.

Year	Sensor/satellite	Day of year
2010	MODIS/Terra	130, 139, 166, 178, 210, 228
	MODIS/Aqua	121, 254
2011	MODIS/Terra	23, 30, 69, 85, 94, 101, 114, 133, 265, 288
	MODIS/Aqua	136, 143, 264, 268, 289

Constrained by these rules and by ground-based measurements for calibration, the number of available clear-sky MODIS/Terra and MODIS/Aqua overpasses was reduced to 23 (16 Terra overpasses and 7 Aqua overpasses) from January 2010 to late October 2011 (see Table 1).

2.3. Theory of SEBAL

2.3.1. Brief overview of SEBAL

SEBAL is a typical one-source energy balance model that utilizes the knowledge of the end-member within the AOI to estimate the sensible heat flux (H) and latent heat flux (LE). For a comprehensive review of the SEBAL model in terms of its inputs, theory, calibration, and validation, please refer to Bastiaanssen et al. (1998, 2005) and Teixeira et al. (2009). Sensible heat flux in the SEBAL is estimated by the commonly used bulk transfer equation,

$$H = \frac{\rho C_p (T_{aero} - T_a)}{R_a} = \rho C_p \frac{dT_s}{R_a} \tag{1}$$

$$R_a = \frac{1}{k^2 u_{200}} \left[\ln\left(\frac{z_2}{z_1}\right) - \psi_h(z_2) + \psi_h(z_1) \right] \left[\ln\left(\frac{200}{z_{om}}\right) - \psi_m(200) \right] \tag{2}$$

where ρ is the air density; C_p is the specific heat of air at constant pressure; T_{aero} is the aerodynamic temperature; T_a is the near-surface air temperature; R_a is the aerodynamic resistance; dT_s is the near-surface air temperature difference; $k = 0.4$ is the von Karman's constant; u_{200} is the wind speed at the blending height (assumed at 200 m above the ground); z_2 and z_1 are fixed at 2 m and 0.1 m in the SEBAL (Bastiaanssen et al., 2005), respectively; Ψ_m and Ψ_h are the stability correction functions for momentum and heat transfer, respectively (Paulson, 1970); z_{om} is the surface momentum roughness height (0.125 times the height of vegetation), estimated in this study from the work of Teixeira et al. (2009) as function of surface albedo and Normalized Difference Vegetation Index (NDVI) if vegetation height is unavailable. Specifically, at the dry pixel, z_{om} is assigned to 0.005 m (Nishida et al., 2003).

One of the greatest difficulties in estimating H using the bulk transfer equation is on the regional near-surface air temperature difference. The SEBAL model is unique in its linear relationship between the near-surface air temperature difference (dT_s) and the surface temperature (T_s) (Fig. 2),

$$dT_s = aT_s + b \tag{3}$$

where a and b are the regression coefficients. Once the dry and wet pixels are determined within the study area, given that $H_{dry} = (R_n - G)_{dry}$, $LE_{dry} = 0$, $dT_{s,dry} = (R_n - G)_{dry}(R_a)_{dry}/(\rho C_p)$ at the dry pixel and $H_{wet} = 0$, $LE_{wet} = (R_n - G)_{wet}$, $dT_{s,wet} = 0$ at the wet pixel, by linearly fitting $(T_{s,wet}, dT_{s,wet})$ and $(T_{s,dry}, dT_{s,dry})$, one can obtain the coefficients in Eq. (3),

$$a = \frac{(R_n - G)_{dry}(R_a)_{dry}/(\rho C_p)}{T_{s,dry} - T_{s,wet}} \tag{4}$$

$$b = -aT_{s,wet} = -\frac{(R_n - G)_{dry}(R_a)_{dry}/(\rho C_p)}{T_{s,dry} - T_{s,wet}} T_{s,wet} \tag{5}$$
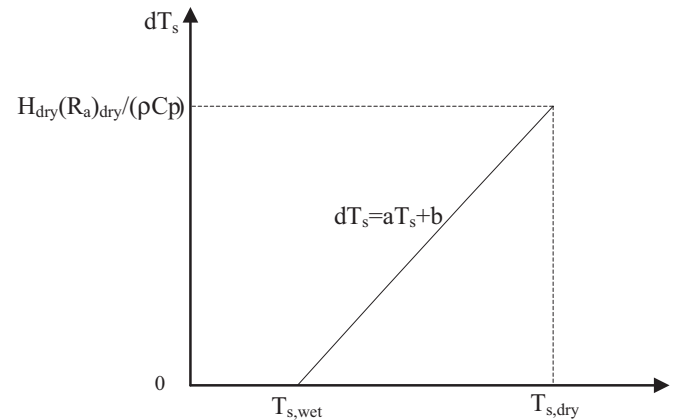

Fig. 2. Schematic illustration of the linear interpolation of the near-surface air temperature difference (dT_s) from the dry and wet pixels in the SEBAL model (H_{dry} and $(R_a)_{dry}$ are the sensible heat flux and aerodynamic resistance at the dry pixel, respectively; ρ is the air density; C_p is the specific heat of air at constant pressure; and $T_{s,wet}$ and $T_{s,dry}$ are the surface temperatures at the wet and dry pixels, respectively).

where $R_n - G$ is the surface available energy; $T_{s,dry}$ and $T_{s,wet}$ are the surface temperatures at the dry and wet pixels, respectively; H, $R_n - G$, LE, dT_s, R_a with subscripts 'dry' and 'wet' indicate the values at the dry and wet pixels, respectively.

2.3.2. Estimation of surface net radiation and soil heat flux

Surface net radiation (R_n) is the sum of the net shortwave and longwave radiations at the ground,

$$R_n = (1 - r)R_g + \varepsilon_s L_d - L_u \tag{6}$$

with

$$L_d = \varepsilon_a \sigma T_a^4 \tag{7}$$

$$L_u = \varepsilon_s \sigma T_s^4 \tag{8}$$

where r is the surface albedo; R_g is the global solar radiation; ε_s is the surface emissivity; L_d is the downward longwave radiation; L_u is the upward longwave radiation; ε_a is the atmospheric emissivity; σ is the Stefan–Boltzmann constant. Tasumi et al. (2008) developed and tested a group of coefficients for MODIS bands 1–7 surface reflectance products (MOD09GA, MYD09GA) to estimate the regional surface albedo. However, the image stripes in band 5 have seriously impaired the practical application of that group of coefficients. In this study, r is derived by fitting 30-min albedo measurement (upward/downward solar radiation) at the Yucheng station to MODIS bands 1–7 surface reflectance products with band 5 removed,

$$r = 0.25125r_1 + 0.17588r_2 + 0.10050r_3 + 0.10050r_4$$
$$+ 0.12060r_6 + 0.25125r_7 \tag{9}$$

where r_i is the surface reflectance in band i ($i = 1, 2, 3, 4, 6, 7$).

Teixeira et al. (2009) have shown that the calibration of G/R_n (the ratio of soil heat flux to surface net radiation) with in situ measurements can greatly improve the estimate of G in the SEBAL model. Therefore, in this study, a step-wise regression is performed between field measurement of G/R_n at the 23 clear-sky MODIS overpass times throughout the year 2010 to late October 2011 and satellite-derived albedo, NDVI, and T_s to obtain the pixel-by-pixel soil heat flux by local calibration (albedo is finally rejected in the step-wise regression),

$$\frac{G}{R_n} = (0.576 - 0.382\text{NDVI} - 0.007(T_s - 273.15)) \tag{10}$$

2.3.3. Selection of dry and wet pixels

The key procedure in implementing the SEBAL model is correctly selecting dry and wet pixels within the AOI that are indicative of the zero ET and maximum ET. However, there has been no consensus in previous studies on how the dry and wet pixels should be selected in the SEBAL model (Bastiaanssen et al., 2005; Long et al., 2011). In this study, the dry and wet pixels are selected by adapting the general rule (a dry pixel is chosen for dry bare soil surfaces and a wet pixel is selected from an irrigated agricultural land or a shallow water body) adopted by a variety of studies to our specific AOI with the aid of a land-use map (Fig. 1b):

(i) If a water body that can be discerned from the satellite data (NDVI < 0, albedo < 0.05) at elevations below 100 m above the sea level (mountainous areas are excluded), the pixel with the lowest temperature in the water body is identified as the wet pixel. Otherwise (e.g., in the dry season), the pixel with the lowest surface temperature and NDVI > 0 in the entire area (for the data at elevations lower than 100 m above the sea level) is selected as the wet pixel;

(ii) The pixel with the highest temperature in the arable land in the AOI is regarded as the dry pixel.

2.4. Theory of the spatial-scale effect

2.4.1. Spatial domain: small to large AOI

For a pixel in a small area of interest (AOI), when the size of the AOI is converted to a large one (Fig. 3a), the surface net radiation and soil heat flux estimated by Eqs. (6) and (10) will remain invariant. However, because of the likely change in the locations of the dry and wet pixels, the linear relationship between dT_s and T_s may be changed, which will influence the estimates of sensible heat flux within the small AOI. Assuming the variation of the stability correction function is small and, thus, that the variation of $R_a/\rho C_p$ is negligible for a given pixel (see Eq. (2)) when the locations of dry and wet pixels are changed, the relative variations of coefficients a and b, surface-air temperature difference (dT_s), and sensible heat flux (H_{SA}) for an intermediate pixel within the small AOI can be written from Eqs. (4), (5), (3), and (1), respectively,

$$\frac{\delta a}{a} = \left(1 + \frac{\delta(R_n - G)_{dry}}{(R_n - G)_{dry}}\right)$$
$$\times \left(\frac{1}{1 + (\delta(T_{s,dry} - T_{s,wet})/(T_{s,dry} - T_{s,wet}))}\right) - 1 \qquad (11)$$

$$\frac{\delta b}{b} = \frac{\delta a}{a} + \frac{\delta T_{s,wet}}{T_{s,wet}} + \frac{\delta a}{a}\frac{\delta T_{s,wet}}{T_{s,wet}} \qquad (12)$$

$$\frac{\delta dT_s}{dT_s} = \frac{\delta a}{a} + \frac{\delta(T_s - T_{s,wet})}{(T_s - T_{s,wet})} + \frac{\delta a}{a}\frac{\delta(T_s - T_{s,wet})}{(T_s - T_{s,wet})} \qquad (13)$$

$$\frac{\delta H_{SA}}{H_{SA}} = \frac{\delta dT_s}{dT_s} \qquad (14)$$

where δx is the variation of variable x ($x = a$, b, dT_s, H_{SA}, similarly hereafter).

As $LE = R_n - G - H$, the variation of latent heat flux (LE_{SA}) is,

$$\delta LE_{SA} = -\delta H_{SA} \qquad (15)$$

2.4.2. Pixel scale: high to low resolution

In addition to the spatial domain effect, how the SEBAL-derived surface energy components are varied poses another challenge when satellite temperature data with different spatial resolutions are employed to model the ET. To quantify the energy transfer due to the pixel-scale effect, some effective variables over the

$n \times n$ high-resolution pixels (corresponding to one targeted low-resolution pixel) are introduced to bridge the differences in scale and in the number of pixels between the high- and low-resolution data. Assuming a low-resolution satellite pixel consisting of $n \times n$ high-resolution pixels ($N = n \times n$, Fig. 3b) and according to the conservation of energy, the effective surface albedo, emissivity, temperature, aerodynamic resistance, and momentum roughness length for the $n \times n$ high-resolution pixels can be derived by the equations below,

Net shortwave radiation:

$$(1 - \bar{r})R_g = \frac{1}{N}\sum_1^N (1 - r_i)R_g \qquad (16)$$

Longwave radiation absorbed by the surface:

$$\bar{\varepsilon}_s \varepsilon_a \sigma T_a^4 = \frac{1}{N}\sum_1^N \varepsilon_i \varepsilon_a \sigma T_a^4 \qquad (17)$$

Upward longwave radiation emitted by the surface:

$$\bar{\varepsilon}_s \sigma \overline{T}_s^4 = \frac{1}{N}\sum_1^N \varepsilon_i \sigma T_{s,i}^4 \qquad (18)$$

Sensible heat flux:

$$\rho C_p \frac{\overline{T}_s - T_a}{\overline{R}_a} = \rho C_p \frac{1}{N}\sum_1^N \frac{T_{s,i} - T_a}{R_{a,i}} \qquad (19)$$

A variable capped with a macron ('‾') symbol in above equations indicates the areal averaged value for the $n \times n$ high-resolution pixels (the effective value, similarly hereinafter, and symbols with a subscript 'i' are for the $n \times n$ high-resolution pixels). From these equations, the effective variables can be written as,

$$\bar{r} = \frac{1}{N}\sum_1^N r_i \qquad (20)$$

$$\bar{\varepsilon}_s = \frac{1}{N}\sum_1^N \varepsilon_i \qquad (21)$$

$$\overline{T}_s = \left[\frac{\sum_1^N \varepsilon_i T_{s,i}^4}{\sum_1^N \varepsilon_i}\right]^{1/4} \qquad (22)$$

$$\frac{1}{\overline{R}_a} = \frac{1}{N}\sum_1^N \frac{T_{s,i} - T_a}{\overline{T}_s - T_a}\frac{1}{R_{a,i}} \qquad (23)$$

Assuming that the atmospheric condition is near neutral and by combining with Eq. (2), Eq. (23) is reduced to,

$$\frac{1}{\ln(200/\overline{z_{om}})} = \frac{1}{N}\sum_1^N \frac{a^H T_{s,i} + b^H}{a^H \overline{T}_s + b^H}\frac{1}{\ln(200/z_{om,i})} \qquad (24)$$

where a^H and b^H are the slope and intercept of the linear equation between dT_s and T_s for the high-resolution satellite data. Presently, new images of temperature and momentum roughness length at low resolution are produced with each pixel data corresponding to the effective values of the $n \times n$ high-resolution pixels.

If there come low-resolution temperature and momentum roughness length (either directly from satellite measurements or from some type of aggregation of high-resolution satellite data) that are, by chance, equivalent to the effective values, the pixel-scale effect from the high- to low-resolution data will be reduced to the spatial domain effect (no variations in surface available energy, surface temperature, momentum roughness, and wind speed),
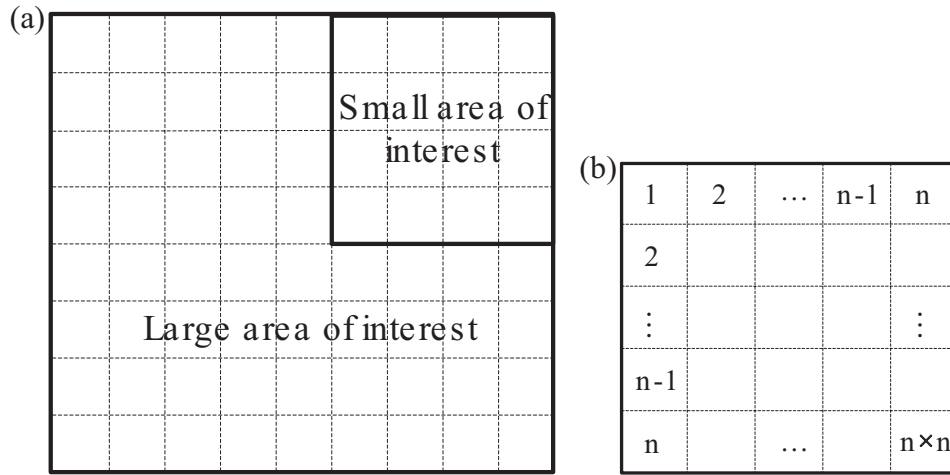
Fig. 3. Schematic illustration of (a) the area of interest shown for both the large and small cases under a given satellite pixel scale within a satellite scene and (b) $n \times n$ high-resolution pixels composing one coarse-resolution pixel.

because, under such a condition, only the linear equation between the dry and wet pixels at the low resolution must be renewed from the original expression at the high resolution. The relative variation of sensible heat flux over the $n \times n$ high-resolution pixels can be expressed as,

$$\frac{\delta \overline{H}}{\overline{H}} = \frac{H^L}{\overline{H}} - 1 = \frac{\delta a^H}{a^H} + \frac{\delta(\overline{T_s} - T_{s,wet}^H)}{(\overline{T_s} - T_{s,wet}^H)} + \frac{\delta a^H}{a^H} \frac{\delta(\overline{T_s} - T_{s,wet}^H)}{(\overline{T_s} - T_{s,wet}^H)} \quad (25)$$

where variables with a 'L' superscript represent the values at coarse resolution (one pixel corresponding to $n \times n$ high-resolution pixels, similarly hereafter) and a 'H' superscript the values at high resolution.

Otherwise, a more general equation can be obtained by,

$$\frac{\delta \overline{H}}{\overline{H}} = \frac{H^L}{\overline{H}} - 1 = \frac{a^L T_s^L + b^L}{a^H \overline{T_s} + b^H} \frac{\ln(200/\overline{z_{om}})}{\ln(200/z_{om}^L)} - 1$$

$$= \frac{(a^H + \delta a^H)(\overline{T_s} + \delta \overline{T_s}) + (b^H + \delta b^H)}{a^H \overline{T_s} + b^H} \frac{\ln(200/\overline{z_{om}})}{\ln(200/(\overline{z_{om}} + \delta \overline{z_{om}}))} - 1 \quad (26)$$

$$LE^L = \overline{LE} + \delta \overline{LE} = \overline{LE} + \delta(\overline{R_n - G}) - \delta \overline{H} \quad (27)$$

2.5. Simulations

The global solar radiation in Eq. (6) was estimated as a function of atmospheric transmissivity (derived as the areal constant from the measurement (the ratio of at-ground to top-of-atmosphere solar radiation) at the Yucheng station), solar zenith angle (MOD11_L2, MYD11_L2), the solar constant, and the eccentricity of the earth. The surface albedo (r) was derived from the MOD09GA and MYD09GA surface reflectance products from Eq. (9). The surface emissivity was estimated by the expression proposed by Liang (2004) from the MODIS emissivities at bands 31 and 32 (MOD11_L2, MYD11_L2). The air temperature and vapor pressure measurements at the Yucheng station were used to estimate the downward longwave radiation.

To evaluate the effect of the size of the AOI, the SEBAL model was run over the small and large AOIs to estimate the coefficients a and b in Eq. (3), and the pixel-by-pixel H and LE for the two AOIs. The variations in a, b, and the pixel-by-pixel H_{LA}/H_{SA} (the ratio of sensible heat flux (H_{LA}) derived using the large AOI to that of the small AOI (H_{SA})) estimated by the SEBAL were used to verify the

analytical equations proposed in Section 2.4.1 that could be independently run after the dry and wet pixels had been selected for the small and large AOIs.

Analogously, the effect of the satellite pixel size was evaluated by running the SEBAL over the AOI with remote sensing data at two different spatial resolutions. The SEBAL-estimated variations in a, b, and the pixel-by-pixel $H^L/\overline{H}$ (the ratio of the low-resolution sensible heat flux (H^L) to that ($\overline{H}$) averaged over the $n \times n$ high-resolution pixels) were used to verify the analytical equations proposed in Section 2.4.2. For a better understanding of the differences in the pixel-scale effect, two cases were presented: (1) the surface temperature, momentum roughness length, emissivity, and albedo at the lower resolution were equal to the corresponding effective values from the $n \times n$ high-resolution satellite data, as explained in Section 2.4.2, and (2) all other possible cases. Specifically, the targeted lower resolution was set to 3 km × 3 km, and the high-resolution satellite data were from 1 km × 1 km MODIS products. For case 2, the low-resolution satellite data were modeled by aggregating 1 km × 1 km MODIS products using the nearest-neighbor method. The area of interest used was the large AOI, as shown in Section 2.1.

3. Results and discussions

3.1. Effect of the size of the AOI

When the size of the AOI is increased, as mentioned in Section 2.4, the surface temperatures at the wet and dry pixels are lowered and raised, respectively. For example, the surface temperatures of the dry pixels in the small AOI are less than or equal to those in the large AOI. Table 2 shows the variations in the locations (also as indicated in Fig. 1b) and temperatures of the dry and wet pixels for the 23 clear-sky MODIS/Terra and MODIS/Aqua overpass times. Of the 23 clear-sky MODIS overpasses, 12 had the wet pixels with the same location and temperature, and one had the same dry pixels for both AOIs. The dry and wet pixels on DOY = 2011268 at the MODIS/Aqua overpass had the same temperatures and locations for both the small and large AOIs. Changes in the surface temperatures of the dry and wet pixels alter the coefficients a and b of the linear equation between T_s and dT_s. Thus, the sensible and latent heat fluxes for a given pixel are varied when the size of the AOI is increased.

The coefficients a (the slope) and b (the intercept) derived by the SEBAL from the linear regression of the dry and wet pixels varied from 0.1663 to 0.7177 and from −48.063 to −216.493, respectively,

Table 2
Dry and wet pixels determined at the MODIS-resolution scale by the rule set in Section 2.3 for the large (data in the upper row for a specific date) and small (data in the lower row for a specific date) areas of interest.

Date	Dry pixel			Wet pixel			Time
	T_s	Longitude[b]	Latitude[c]	T_s	Longitude	Latitude	
2010130[a]	313.42	344105	4089702	289.20	600105	4208702	
	309.82	420105	4094702	289.20	600105	4208702	
2010139	317.28	358105	4095702	289.56	490105	3866702	
	313.06	438105	4141702	293.52	605105	4208702	
2010166	316.78	314105	3903702	297.96	428105	3978702	
	314.72	543105	4221702	299.80	604105	4211702	
2010178	315.56	504105	3824702	298.92	429105	3980702	
	312.76	630105	4215702	299.96	489105	4218702	
2010210	312.52	655105	4143702	301.46	426105	3977702	
	312.06	438105	4141702	302.44	600105	4207702	
2010228	309.22	465105	3917702	300.10	526105	3826702	
	309.14	558105	4222702	301.64	487105	4217702	
2011023	280.90	532105	3859702	267.50	601105	4207702	
	280.16	435105	4148702	267.50	601105	4207702	
2011030	285.34	314105	4101702	269.30	601105	4205702	
	283.64	512105	4205702	269.30	601105	4205702	Data at Terra overpass time
2011069	304.22	311105	4143702	277.86	378105	4163702	
	299.60	504105	4206702	279.50	603105	4207702	
2011085	304.14	336105	4085702	280.94	604105	4210702	
	299.70	452105	4223702	280.94	604105	4210702	
2011094	308.04	448105	4260702	284.62	488105	4217702	
	307.20	462105	4241702	284.62	488105	4217702	
2011101	311.18	447105	4261702	283.84	604105	4208702	
	310.68	454105	4239702	283.84	604105	4208702	
2011114	308.04	449105	4240702	286.58	605105	4208702	
	307.44	577105	4061702	286.58	605105	4208702	
2011133	314.64	338105	4098702	290.80	605105	4208702	
	310.16	419105	4093702	290.80	605105	4208702	
2011265	308.02	316105	3975702	292.74	528105	3828702	
	304.96	516105	4065702	293.02	604105	4208702	
2011288	303.72	311105	4160702	287.96	603105	4208702	
	300.02	456105	4073702	287.96	603105	4208702	
2010121	321.04	344105	4147702	288.04	486105	4217702	
	314.10	452105	4239702	288.04	486105	4217702	
2010254	312.34	532105	4246702	297.02	498105	3859702	
	309.82	552105	4220702	298.66	600105	4207702	
2011136	320.84	402105	4223702	293.44	524105	3827702	
	318.08	506105	4219702	295.36	603105	4207702	
2011143	315.84	450105	4245702	292.18	429105	3977702	Data at Aqua overpass time
	313.56	490105	4237702	292.78	487105	4217702	
2011264	310.88	316105	3974702	292.52	524105	3828702	
	305.38	645105	4216702	293.24	488105	4217702	
2011268	307.72	606105	4215702	292.82	487105	4217702	
	307.72	606105	4215702	292.82	487105	4217702	
2011289	311.22	365105	4058702	289.08	604105	4208702	
	308.36	488105	4149702	289.08	604105	4208702	

[a] The day 130 of year 2010.
[b] Longitude coordinate in UTM projection (zone number 50N).
[c] Latitude coordinate in UTM projection (zone number 50N).

for the small AOI. For the large AOI, the coefficients (a' and b') varied from 0.1474 to 0.5580 and from −42.600 to −144.301, respectively. In most cases, both the slope and intercept (absolute value) have decreased with relative variations less than zero when the size of the AOI was increased from small to large. Two exceptions occurred on DOY = 2011023 at the MODIS/Terra overpass and on DOY = 2011268 at the MODIS/Aqua overpass. The maximum absolute relative variations of the SEBAL-derived coefficients a ($\delta a/a$) and b ($\delta b/b$) were 37% and 37.8%, respectively. Eqs. (11), (12), and (13) imply that when the AOI changes, (1) if there are no variations in the locations of dry and wet pixels, a and b will not change, and (2) if only the wet pixel is unchanged, $\delta b/b$ and the relative changes in dT_s can be simplified as $\delta a/a$. The first implication was satisfied for the unchanged dry and wet pixels on DOY = 2011268, and 12 DOYs met the second in the 23 MODIS overpasses. The variations in a and b given by the analytical Eqs. (11) and (12) were comparable to the SEBAL-derived values. The maximum bias (absolute value)

between the deduced $\delta a/a$ and $\delta b/b$ and SEBAL-derived values was limited to −0.084. However, the relative difference was as high as 127% on DOY = 2011023. The analytical equation seems to be able to depict the overall variations in a and b, but some exceptions may also occur, especially when a and b are small.

Fig. 4 illustrates the variations of the ratio of H_{LA} to H_{SA} with surface temperature as predicted by Eq. (14) for four representative clear-sky MODIS/Terra and MODIS/Aqua overpass times [$H_{LA}/H_{SA} = 1 + \delta a/a + \delta T_{s,wet}/(T_s - T_{s,wet}) + \delta a/a \times \delta T_{s,wet}/(T_s - T_{s,wet})$], where H_{SA} is the sensible heat flux within the small AOI using the small AOI to determine the dry and wet pixels, and H_{LA} is the sensible heat flux for the same pixel, but derived using the large AOI]. The four overpass times represent typical cases characterized by (1) no variation in the wet pixels (DOY = 2010130 and 2011023), (2) increased and decreased temperatures of the dry and wet pixels, respectively (DOY = 2010139), (3) increased a and b (DOY = 2011023), and (4) no variation in either the dry
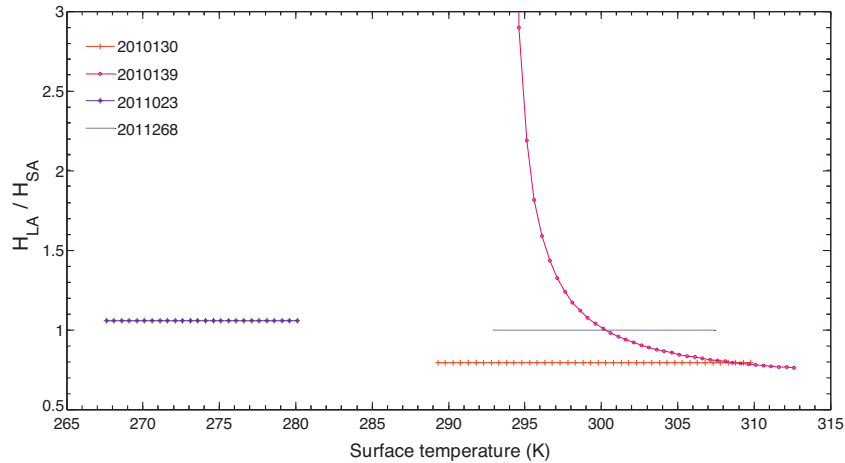
Fig. 4. Variation of the ratio of H_{LA} to H_{SA} with surface temperature as predicted by the proposed analytical Eq. (14) at four representative clear-sky MODIS/Terra and MODIS/Aqua overpass times ($H_{LA}/H_{SA} = 1 + \delta a/a + \delta T_{s,wet}/(T_s - T_{s,wet}) + \delta a/a \times \delta T_{s,wet}/(T_s - T_{s,wet})$), where H_{SA} is the sensible heat flux derived by the SEBAL using the small AOI, and H_{LA} is the sensible heat flux for the same pixel but derived using the large AOI. For each of the curves, the surface temperature was varied from the temperature at the wet pixel to that at the dry pixel for small AOI).

or wet pixels (DOY = 2010268). These curves of H_{LA}/H_{SA} as shown in Fig. 4 are either power functions or constant functions when the surface temperature varies from the temperature of the wet pixel ($T_{s,wet}$) to that of the dry pixel ($T_{s,dry}$). If the temperature of the wet pixel is not varied when shifting from the small to the large AOI, the pixel-by-pixel sensible heat flux (H_{LA}) within the small AOI using the large AOI for determining the dry and wet pixels can be expressed as $\delta a/a$ multiplied by the sensible heat flux (H_{SA}) at the same pixel derived using the small AOI (see Eqs. (13) and (14)). If the temperature of the wet pixel is changed, the curve (H_{LA}/H_{SA} is artificially controlled to be between 0.5 and 3) will approach infinity and reach a minimum when the surface temperature approximates $T_{s,wet}$ and $T_{s,dry}$, corresponding to ~0 and the maximum sensible heat flux, respectively. In most cases, the sensible heat flux derived using the large AOI is smaller than that derived using the small AOI ($H_{LA}/H_{SA} < 1$), particularly for cases in which the wet pixels are unchanged for the small and large AOIs.

The pixel-by-pixel H_{LA}/H_{SA} estimated using the simplified analytical equation is verified by comparison with the SEBAL estimate as shown in Fig. 5 on four DOYs (2010130, 2010139, 2011023, and 2011268). Fig. 5 shows that in all four cases Eq. (14) can model the variation of sensible heat flux when the size of the AOI is increased. The analytically estimated H_{LA}/H_{SA} equal to a constant value of $1 + \delta a/a$ may be either larger or smaller than the SEBAL-derived value when the wet pixel does not vary, depending on the change in a. The maximum relative difference between the analytically estimated H_{LA}/H_{SA} and the SEBAL-derived value for DOY = 2010130 and DOY = 2011023 was generally no more than 3.6% and 7.0%, respectively, which indicates that for an invariant wet pixel, the constant value may better model the variation in sensible heat flux if the coefficient a is decreased. The results on DOY = 2011023 also demonstrate that the large differences between the SEBAL-derived coefficients a and b and those given by the analytical equations do not necessarily significantly bias the estimated H_{LA}/H_{SA}. The nearly constant H_{LA}/H_{SA} on DOY = 2010130 ($H_{LA}/H_{SA} < 1$) and DOY = 2011023 ($H_{LA}/H_{SA} > 1$) was also shown in Fig. 9 of Long et al. (2011). The case on DOY = 2010139 had the largest difference (0–∞, from a theoretical viewpoint) between the H_{LA}/H_{SA} values derived by the SEBAL and by the simplified analytical equation. As mentioned above, H_{LA}/H_{SA} for such a case would approach a very large value depending on how close the surface temperature is to $T_{s,wet}$ (the range of the ordinate was limited

between 0 and 3 in Fig. 5b). The shape of the curve was very well modeled. The difference in H_{LA}/H_{SA} between the SEBAL-derived value and that from the analytical equation, which could cause an appreciable difference in the sensible heat flux, approximated 5.0% at the temperature close to $T_{s,dry}$. As expected, the H_{LA}/H_{SA} value on DOY = 2011268 was perfectly modeled when the dry and wet pixels remained invariant.

The outlier points in Fig. 5 correspond to the few pixels that have inconsistent surface temperatures in the large and small AOIs. Ideally, when the small AOI is changed to the large one, surface temperature for a given pixel in the small AOI will remain invariant. However, when the small and the large AOIs were obtained by sub-setting MOD11_L2 and MYD11_L2 land surface temperature products, several pixels in the small AOI had different temperatures with the corresponding pixels in the large AOI due to the resampling effect, causing the deviation of H_{LA}/H_{SA} at the outlier points from that at the remaining pixels as shown in Fig. 5.

3.2. Effect of the size of the pixel scale

3.2.1. Case one

When low-resolution variables such as surface temperature, albedo, emissivity, aerodynamic resistance, and momentum roughness length are derived from the effective values of the corresponding $n \times n$ high-resolution data, the complexity of the spatial effect of the pixel size on the SEBAL model is reduced significantly. Under these circumstances, the SEBAL-derived surface available energy remains constant, the sensible heat flux varies only because the coefficients a and b must be recalculated for the lower resolution, and the variation in latent heat flux is complementary to that of the sensible heat flux.

The albedo, emissivity, temperature, aerodynamic resistance, and momentum roughness length at each of the 3 km × 3 km pixels were equivalent to the effective values estimated by Eqs. (20)–(24), and they varied between the minimum and maximum of the corresponding nine 1 km × 1 km high-resolution data points. This aggregation method using the surface energy conservation smooths and compresses the spatial distribution of surface temperature (see Fig. 6 as an example). It varies the locations of the dry and wet pixels in the large AOI unless the high-resolution data are homogeneous, causing the temperature to decrease or remain unchanged for dry pixels and to increase or remain unchanged for wet pixels. When high-resolution data were changed to
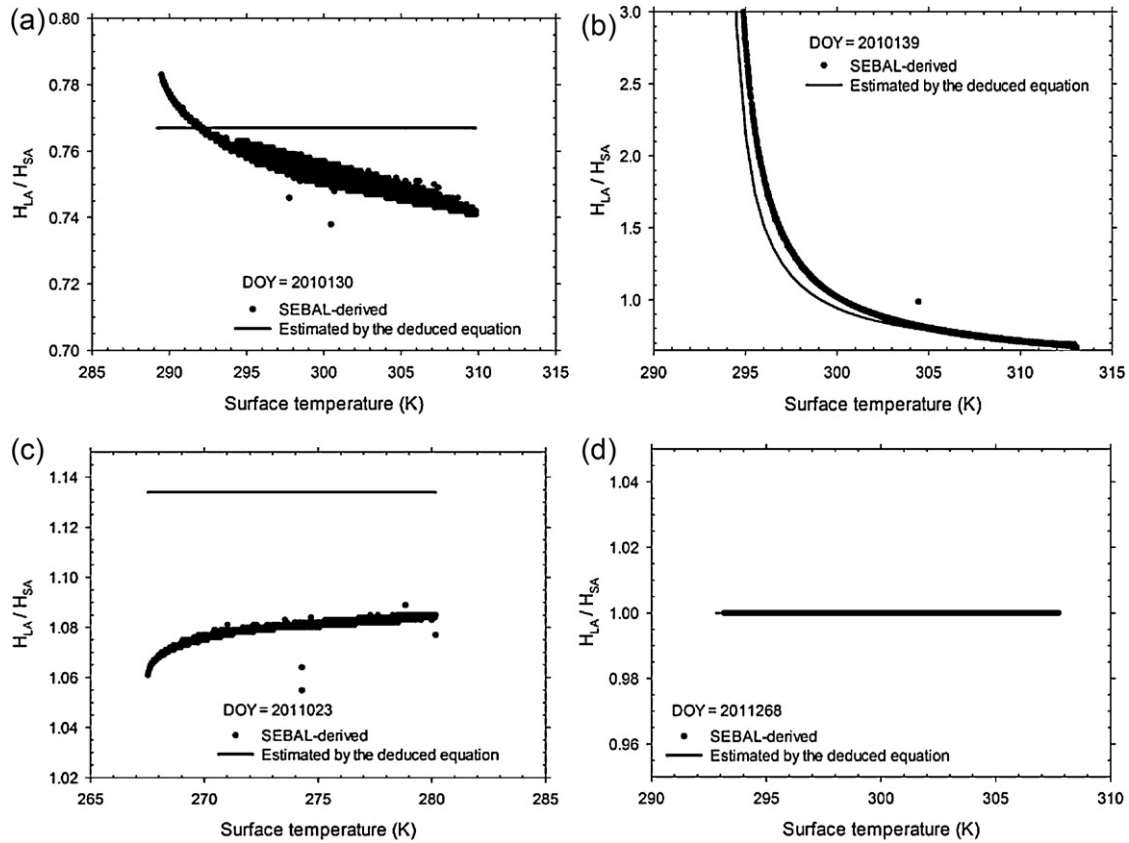
Fig. 5. Comparison of the pixel-by-pixel H_{LA}/H_{SA} estimated by the simplified analytical equation with that obtained from the SEBAL estimate on four typical days of year (a) 2010130 (no variation in the wet pixels), (b) 2010139 (increased and decreased temperatures of the dry and wet pixels, respectively), (c) 2011023 (increased coefficients a and b), and (d) 2011268 (no variation in either the dry or wet pixels) (H_{SA} is the sensible heat flux within the small AOI derived by the SEBAL using the small AOI to determine the dry and wet pixels, and H_{LA} is the sensible heat flux for the same pixel but derived using the large AOI).
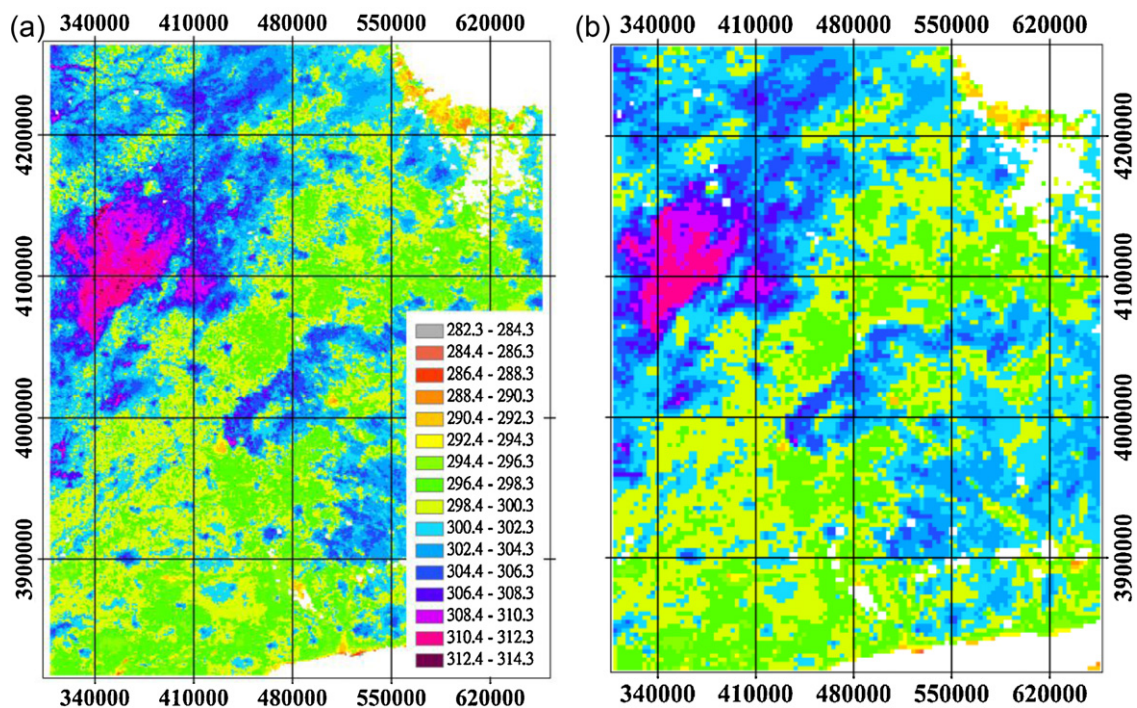

Fig. 6. Spatial distribution of surface temperature (unit: K) on DOY = 2010130 over the large AOI (a) from the original 1 km × 1 km MODIS/Terra product and (b) after aggregation to 3 km × 3 km resolution scale under the conservation of surface energy as estimated by Eq. (22).

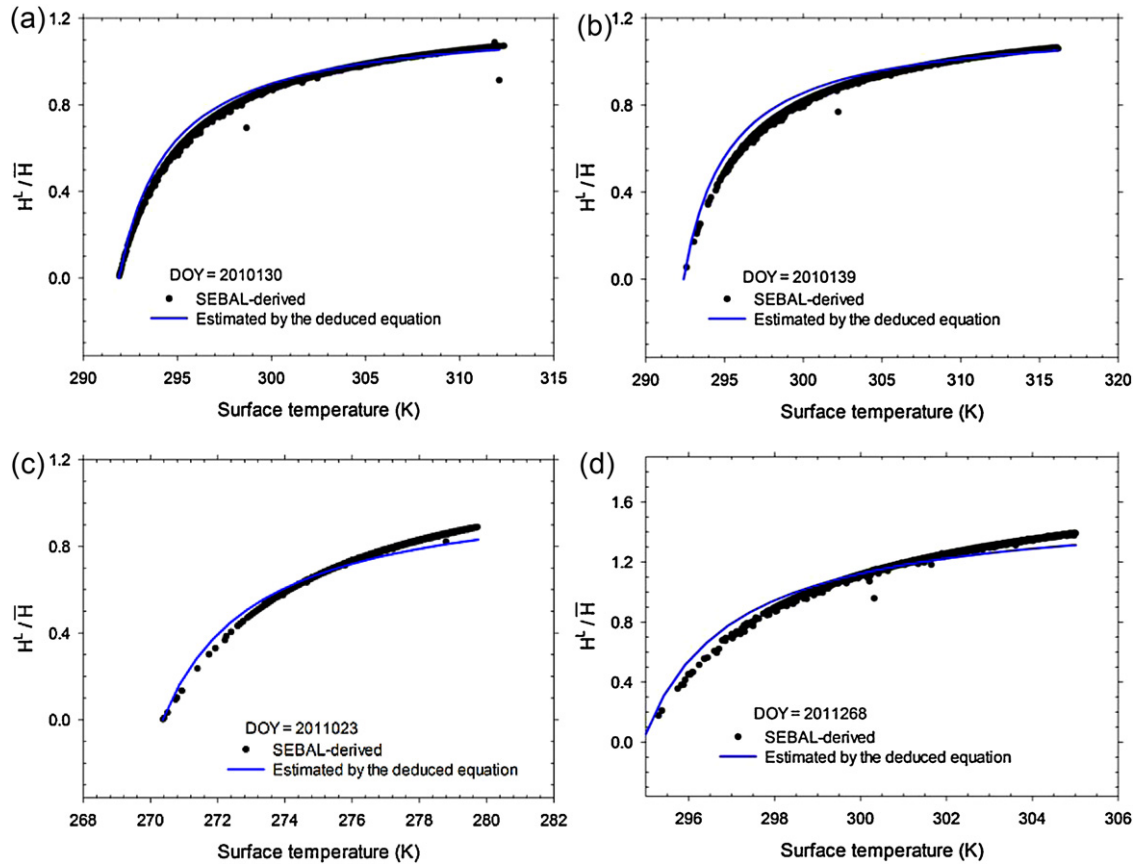**Fig. 7.** Comparison of pixel-by-pixel $H^L/\bar{H}$ estimated by SEBAL with that given by our analytical equation ($H^L/\bar{H}$ is the ratio of the sensible heat flux (H^L) at the 3 km × 3 km coarse resolution with the temperatures aggregated from the 1 km × 1 km high-resolution data according to the conservation of surface energy to the sensible heat flux ($\bar{H}$) averaged over the nine high-resolution pixels) on four typical days of year (a) 2010130, (b) 2010139, (c) 2011023 and (d) 2011268.

low-resolution, the temperatures of the dry pixels in the 23 MODIS overpasses decreased to between 279.75 K on DOY = 2011023 and 318.13 K on DOY = 2011136, whereas the temperatures of the wet pixels increased to between 270.36 K on DOY = 2010023 and 301.89 K on DOY = 2010210. The difference between the temperatures of the dry pixel and of the wet pixel varied from 9.12 K on DOY = 2010228 to 33 K on DOY = 2010121 for the high-resolution data, whereas it decreased from 6.22 K on DOY = 2010210 to 25.70 K on DOY = 2010121 for the aggregated low-resolution data.

The results obtained from the SEBAL and the analytical analyses demonstrated that the slope and intercept increased when the effective surface temperature for the nine 1 km × 1 km high-resolution pixels was used to determine the dry and wet pixels. After the aggregation, the slope (a^L) and intercept (b^L) from the SEBAL at the lower resolution increased to between 0.1796 on DOY = 2011136 and 0.8904 on DOY = 2010210 at the MODIS/Aqua overpass and from −52.783 on DOY = 2011136 to −268.302 on DOY = 2010210 at the MODIS/Terra overpass, respectively. Relative variation of the slope increased by a similar magnitude to that of the intercept for each of the 23 overpass times. The maximum and minimum relative variations estimated by the SEBAL were ∼88% on DOY = 2011265 and 6% on DOY = 2011133. The proposed analytical Eqs. (11) and (12) well reproduced the SEBAL-derived variations in the slope and intercept with relative differences generally less than 20%. Exceptions occurred on DOY = 2011023 and DOY = 2011094 at the MODIS/Terra overpass times with corresponding biases of approximately 58% and 24%, respectively. These exceptions were primarily caused by the variations of the stability correction function that have been overlooked in deducing

the analytical equations. As the analytical equations proposed to estimate the variations of the slope and intercept of the linear regression between near-surface air temperature difference and surface temperature were based on the assumption that variation of the stability correction function at the dry pixel could be negligible, the analytical equations would fail to produce reliable estimates when the variation of the stability correction function was non-negligible.

As explained in Section 2.4.2, when the low-resolution data are equal to the effective values of the corresponding $n \times n$ high-resolution pixels, the spatial-scale effect on the SEBAL-derived sensible heat flux occurs only because the dry and wet pixels at the lower resolution must be re-determined, and the slope and intercept of the linear regression may be altered. The sensible heat flux for the low-resolution pixels can be deduced from the variations in the slope and intercept if we assume that the variations in the stability correction functions for the momentum and heat transfer are negligible. Fig. 7 compares the pixel-by-pixel $H^L/\bar{H}$ estimated by the simplified analytical equation to that obtained from the SEBAL estimate for four DOYs (2010130, 2010139, 2011023, and 2011268), where H^L is the sensible heat flux for the low-resolution data within the large AOI derived by the SEBAL using the effective variables as inputs and $\bar{H}$ is the averaged sensible heat flux over the nine 1 km × 1 km pixels derived using the original MODIS product to determine the dry and wet pixels. The concentration of pixel-by-pixel SEBAL-derived $H^L/\bar{H}$ on a line with varying surface temperatures in Fig. 7 demonstrates the validity of our assumption. The $H^L/\bar{H}$ curve is a convex, monotonically increasing function of surface temperature. With the increase in surface temperature
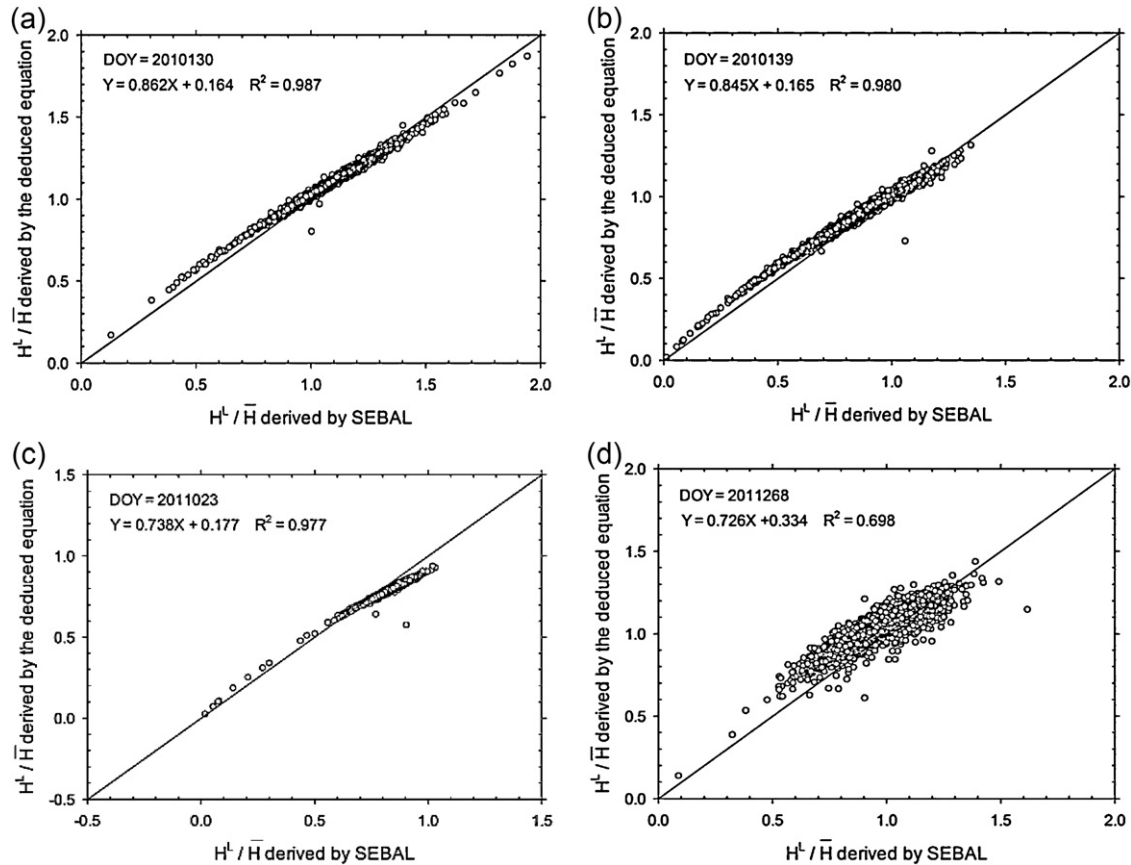
Fig. 8. Comparison of the pixel-by-pixel $H^L/\bar{H}$ (ratio of the sensible heat flux (H^L) at the 3 km × 3 km resolution scale to the corresponding effective value ($\bar{H}$) over the nine 1 km × 1 km high-resolution pixels) given by the analytical equation with those derived by the SEBAL (the nearest neighbor resampling method was applied to generate the coarse-resolution data) on four typical days of year (a) 2010130, (b) 2010139, (c) 2011023, (d) 2011268.

from $T_{s,wet}$ to $T_{s,dry}$ for the low-resolution data, $H^L/\bar{H}$ increases gradually from 0 to a near-constant positive value, but the growth rate decreases. For $H^L/\bar{H} < 1$, the sensible heat flux derived from the low-resolution data becomes lower than the average for the 3 × 3 high-resolution pixels when SEBAL is applied to the high- and low-resolution data. Depending on the magnitude of the variations in the intercept and slope for the low-resolution data and variations in surface temperature for high-resolution data, the sensible heat flux becomes higher than the average when $H^L/\bar{H} > 1$. Overall, the proposed analytical equation well reproduced the $H^L/\bar{H}$ values derived by the SEBAL model on these four typical days. Specifically, the SEBAL-derived $H^L/\bar{H}$ was systematically overestimated by up to 15% (DOY = 2011268) and underestimated by up to 7.6% (DOY = 2011023) when the surface temperature approached the values at the wet and dry pixels, respectively.

The outlier points in Fig. 7 correspond to the pixel at the Yucheng station (the left outlier in Fig. 7a, the outliers in Fig. 7b–d) and the location at the dry pixel (the right outlier in Fig. 7a). Theoretically, when low-resolution variables such as surface temperature, albedo, emissivity, aerodynamic resistance, and momentum roughness length are derived from the effective values of the corresponding high-resolution data, there should be no outliers in the SEBAL-derived $H^L/\bar{H}$. However, because momentum roughness length was calculated as a fraction of vegetation height at the Yucheng station and fixed to be 0.005 at the dry pixel to estimate the sensible heat flux in the SEBAL model at both the high and low resolution scales, as pointed out in Section 2.3.1, which meant that the momentum roughness length at the Yucheng station and at the dry pixel over the coarse resolution scale did not equal the effective values of

the corresponding nine 1 km × 1 km high-resolution pixels, there must be outliers in the SEBAL-derived $H^L/\bar{H}$. These outliers can be avoided by using effective momentum roughness length at the Yucheng station and at the dry pixel to estimate sensible heat flux from the SEBAL at the low resolution scale.

3.2.2. Case two

In most cases, the surface temperature, albedo, emissivity, aerodynamic resistance, and momentum roughness length from the low-resolution satellite data are not equal to the effective values at the corresponding $n × n$ high-resolution pixels. In this case, the spatial effect of the size of the satellite pixels on the SEBAL must account for the effects of variations in these variables on the surface available energy, sensible heat flux, and latent heat flux. The variables acquired simultaneously by high- and low-resolution sensors should ideally have the same sensor view zenith and azimuth angles, facilitating the study of differences in the surface energy components derived by the SEBAL resulting from the spatial effect. Constrained by the available satellite data, we attempted to model the 3 km × 3 km low-resolution data (surface net radiation, soil heat flux, albedo, emissivity, NDVI, and surface temperature) by resampling the original 1 km × 1 km MODIS product to a 3 km × 3 km grid size as an example using the nearest neighbor (NN) method. This type of aggregation selected the value of the nearest point and did not consider the effect of the surrounding eight pixels. Although this may be invalid under some conditions, it did not hinder the evaluation of the spatial effect of the pixel size on the SEBAL model.

In some cases, the surface temperature was the same for dry or wet pixels determined from the aggregated 3 km × 3 km map

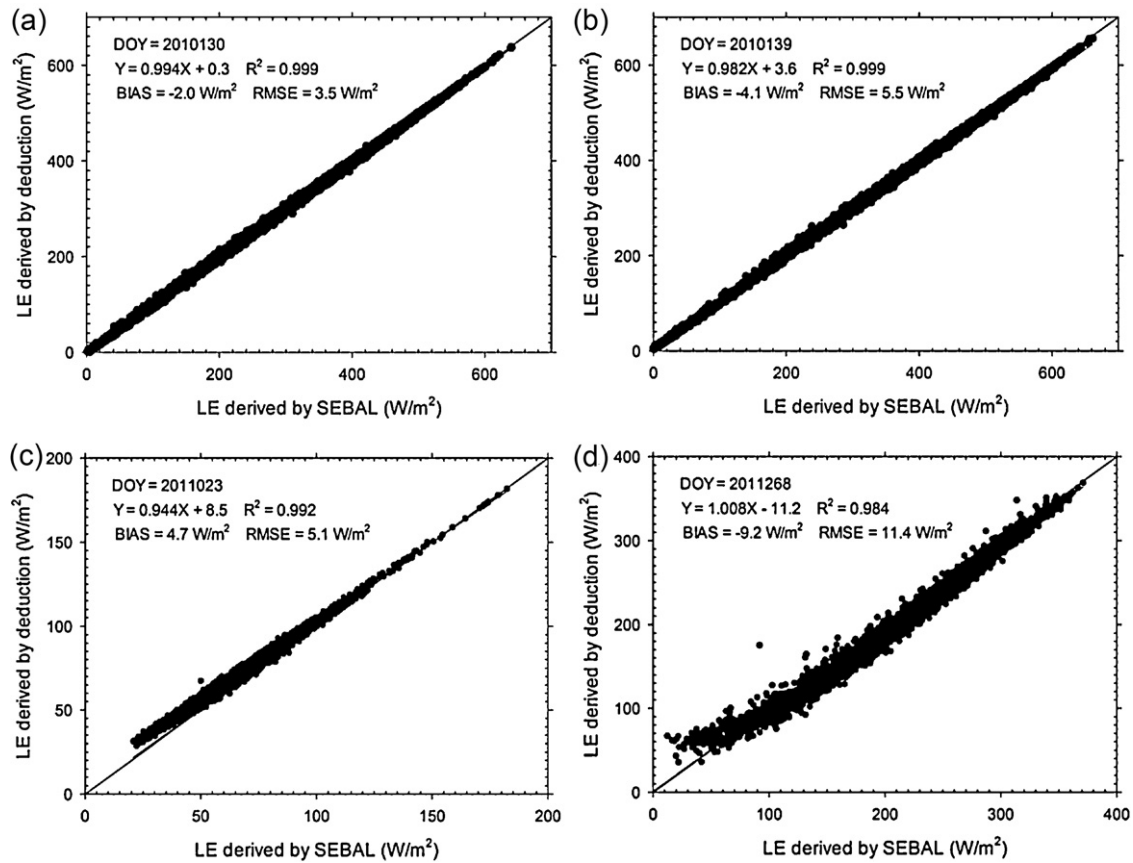**Fig. 9.** Comparison of the pixel-by-pixel *LE* (*LE^L* as shown in Eq. (29) in Section 2.2.2) deduced analytically at the 3 km × 3 km resolution scale with those derived by the SEBAL (the nearest neighbor resampling method was applied to generate the coarse-resolution data) on four typical days of year (a) 2010130, (b) 2010139, (c) 2011023 and (d) 2011268.

using the NN resampling method and from the original 1 km × 1 km MODIS product. This occurred for dry pixels on DOY = 2011085 for the Terra overpass and DOY = 2011136 for the Aqua overpass, and for wet pixels on DOY = 2010130, 2010178, 2010210 for the Terra overpass and DOY = 2011136 for the Aqua overpass. Under these conditions, the slope (*a*) and intercept (*b*) of the linear regression in Eq. (3) were not influenced by the shift from high- to low-resolution data (see Eqs. (11) and (12)). Constant $T_{s,dry}$ and $T_{s,wet}$ values may occur when the sub-pixels are homogeneous at the lower resolutions. However, $T_{s,dry}$ and $T_{s,wet}$ for the low-resolution map are generally between the corresponding $T_{s,dry}$ and $T_{s,wet}$ derived for the high-resolution image, as expected.

The slope (a^L) and intercept (b^L) at the 3 km × 3 km resolution varied from 0.1621 to 0.7403 and from −33.878 to −233.165, respectively. The relative variations in slope and intercept increased with similar magnitude by a maximum of ∼55% in 20 of the 23 MODIS overpasses. Three exceptions occurred for the Terra overpasses on DOY = 2011023, 2011030, and 2011133, with a maximum decrease of ∼4%. Additionally, both the slope and intercept remained constant on DOY = 2011136 for the Aqua overpass, which was caused by the invariant dry and wet pixels that were a result of the NN resampling method. The slope and intercept for the low-resolution data aggregated by the NN resampling method depend on the spatial distribution and magnitude of the heterogeneity of surface variables at the original high resolution. If the sub-heterogeneities at the dry and wet pixels are negligible at the lower resolution (the NN method can be regarded as a special case) and the locations of dry and wet pixels are not altered when the SEBAL for the high-resolution data is applied to the low-resolution satellite data, the slope and intercept remain constant.

Otherwise, these two coefficients are likely to change. The maximum bias in the relative variations in the slope (*a*) and intercept (*b*) between Eqs. (11) and (12)-deduced and the SEBAL-derived values was 0.107 on DOY = 2011265. Similar to case 1, the overestimation could maximally approximate by ∼249% on DOY = 2011023, when the variations in *a* and *b* were small. Overall, the relative variations given by the analytical equations were in good agreement with those derived by the SEBAL model.

The variations in the SEBAL-derived areal-averaged sensible heat flux when shifting from high- to low-resolution satellite data are controlled by the magnitude of the deviation of surface temperature, the surface available energy at the dry pixels, and the momentum roughness from the corresponding effective values and by the variations of coefficients *a* and *b* as shown in Eq. (26). Fig. 8a–d compare the pixel-by-pixel $H^L/\bar{H}$ (the ratio of the sensible heat flux (H^L) at the 3 km × 3 km low resolution to the corresponding average ($\bar{H}$) over the nine 1 km × 1 km high-resolution pixels) from the analytical equation with values from the SEBAL using the NN resampling method to generate low-resolution data on DOYs = 2010130, 2010139, 2011023, and 2011268, respectively. The results for DOY = 2010130, 2011139, and 2011023 agreed well, with a coefficient of determination (R^2) of ∼0.98. Systematic overestimations become underestimations when $H^L/\bar{H}$ varied from 0 to its maximum for the four DOYs. To guarantee the validity of the surface variables/parameters at the low-resolution scale, the data at each of the nine 1 km × 1 km high-resolution MODIS pixels should be cloud-free, which decreased the number of valid pixels to <65% on DOY = 2011023 at the low-resolution scale within the large AOI and >90% for the other three days (see Fig. 8). The scatter in the data was relatively large, with $R^2 = 0.698$ on DOY = 2011268 for a

comparison of the SEBAL-derived $H^L/\bar{H}$ and analytically deduced values (Fig. 8d). The non-negligible stability correction function caused by the large surface heterogeneity in the nine 1 km × 1 km MODIS pixels during the harvest of the summer crop may contribute to this scatter of $H^L/\bar{H}$. Approximately 11% of the total pixels on DOY = 2011268 had an absolute relative bias of 10–20% and the remaining 89% had less than 10% bias. These uncertainties propagated to the estimation of the sensible heat flux using the analytical equation.

Similar to Fig. 7, Fig. 8 also has some outlier points that correspond to the location at the Yucheng station (the outlier with the second largest deviation in Fig. 8a–d) and at the dry pixel (the outlier with the largest deviation in Fig. 8a–d). These outliers appear because we have not used the effective momentum roughness length at the dry pixel or at the Yucheng station, as explained earlier on the outliers in Fig. 7.

The latent heat flux (*LE*) in the SEBAL is estimated as the residual of the surface energy budget. Therefore, variations in the SEBAL-derived *LE* require quantified variations of the surface available energy and the sensible heat flux, and they can be evaluated using Eq. (27), as shown in Section 2.4.2. The pixel-by-pixel *LE* deduced at the 3 km × 3 km resolution scale is compared with that derived using the SEBAL (the NN resampling method is applied to generate the low-resolution data) in Fig. 9a–d for typical DOYs (2010130, 2010139, 2011023, and 2011268, respectively) to obtain a better understanding of the spatial effect of pixel size. For each of the four days, the *LE* given by the analytical equation was in good agreement with the results of the SEBAL model at the 3 km × 3 km resolution scale, with a R^2 greater than 0.98. Both the absolute bias and RMSE were less than 6 W/m^2 on DOYs = 2010130, 2010139, and 2011023 and ~12 W/m^2 on DOY = 2011268. The lack of a SEBAL-derived LE within 0–20 W/m^2 on DOY = 2011023 could be explained by the lower number of valid data (<60%) and the relatively small momentum roughness length (low NDVI and high albedo). The relatively large difference on DOY = 2011268 was due to the scatter in the comparison of the SEBAL-derived $H^L/\bar{H}$ with the results of the analytical equation because latent heat flux was estimated as the residual of surface energy balance in the SEBAL. Thus, the proposed equations in Section 2.4 can well trace the variations in the SEBAL-derived sensible and latent heat fluxes caused by the spatial effect of the sizes of the AOI and satellite pixels.

4. Summary and conclusions

The spatial effect of the sizes of the area of interest (AOI) and satellite pixels was comprehensively evaluated by applying the SEBAL to MODIS/Terra and MODIS/Aqua data at 23 clear-sky overpasses covering different soil water contents and crop growth stages from January 2010 to late October 2011. Considering the uncertainty in the estimated surface net radiation and the limited validation of the surface energy components (due to a lack of ground-based measurements of net radiation, soil heat flux, sensible heat flux, and latent heat flux) over the mountainous area, we chose to exclude southeastern undulating area of the large AOI and limit our study to the relatively flat area, which is thought to have little influence on the quantification of the spatial-scale effect of the SEBAL.

In contrast to previous studies that evaluate the spatial-scale effect of the SEBAL model using a simple comparison, this paper proposes generalized analytical equations to reveal the mechanism of the scaling transfer of the SEBAL model. These equations have been verified by comparing the variations of the coefficients a and b in Eq. (3) and pixel-by-pixel sensible and latent heat fluxes (Eqs. (14) and (25)–(27)) with those estimated by directly implementing the SEBAL model. From the proposed analytical

equations in Section 2.4, one can understand thoroughly and straightforward how the variations in the intermediate variables propagate to the resultant surface energy components and under which circumstances the sensible heat flux will be overestimated/underestimated/unaltered, even without running the SEBAL model when the AOI or the pixel size of the satellite data is changed. These equations can be used to predict how the surface energy components will vary for a change in the size of the AOI and satellite pixels, as long as the transfer of the dry and wet pixels and the relative deviation of the effective variables are known. This predictive capability can simplify the evaluation of the spatial-scale effect of the SEBAL model and sets this study apart from previous studies. In the investigation of the spatial effect of the size of the satellite pixels on the SEBAL, the quantitative relationship of the intermediate variables at the low- and high-resolutions is defined by introducing effective values for the $n \times n$ high-resolution pixels (corresponding to a targeted low-resolution pixel), which successfully bridges the difference in both the scale and the number of pixels between the high- and low-resolution data.

The following conclusions are made regarding the effect of the size of the AOI on the SEBAL model: (1) if the locations of dry and wet pixels do not vary, the sensible heat fluxes derived using the large AOI (H_{LA}) and small AOI (H_{SA}) are equal ($H_{LA}/H_{SA} = 1$), (2) if only the surface temperatures of the wet pixels do not vary, H_{LA} derived using the large AOI is greater than H_{SA} when the coefficient a is increased, and vice versa ($H_{LA}/H_{SA} = 1 + \delta a/a$), and (3) if the dry pixels do not vary or if both the dry and wet pixels vary, then H is affected by both the coefficient a and the difference between T_s and $T_{s,wet}$. In the last case, H_{LA}/H_{SA} decreases at a slowing rate from ~∞ to a certain positive value as the surface temperature increases from $T_{s,wet}$ to $T_{s,dry}$ (both temperatures are for the small AOI).

Analogously, the spatial-scale effect of the satellite pixels on the SEBAL model is summarized as:

(1) When the low-resolution surface temperature, albedo, emissivity, aerodynamic resistance, and momentum roughness length are equivalent to the effective values of the corresponding $n \times n$ high-resolution pixels, the relative variations in H can be estimated by the relative variations of the coefficient a and the difference between the effective temperature and $T_{s,wet}$ at the original wet pixel. The value of $H^L/\bar{H}$ (the ratio of the sensible heat flux (H^L) estimated by the SEBAL using the low-resolution effective data to the averaged value ($\bar{H}$) over the corresponding $n \times n$ high-resolution pixels) grows gradually from 0 to a specific near-constant positive value, but the growth rate decreases. Under these circumstances, the surface available energy remains constant, and the variation of the latent heat flux is complementary to that of the sensible heat flux.

(2) When the coarse satellite data are not equal to the effective values at the corresponding $n \times n$ high-resolution pixels, the spatial effect of the size of the satellite pixel on the SEBAL must consider the variations of these variables for the surface available energy, the sensible heat flux and latent heat flux. The variation in the sensible heat flux can be expressed by a general analytical function of the changes in the coefficients a and b, in the difference between the surface temperature and $T_{s,wet}$ at the low-resolution scale, in the difference between the effective temperature and $T_{s,wet}$ at the higher resolution, and the change in the effective momentum roughness length.

Additional study areas with different levels of heterogeneity may reinforce the findings of this study. The AOI in this study primarily has a winter wheat-summer corn crop rotation, and it covers a broad range of vegetation growth stages and vegetation cover/soil wetness conditions from 2010 through late October 2011. Therefore, our study represents a variety of meteorological

and surface vegetation/soil moisture conditions. When the size of the AOI changes, the land cover type and the range of the elevation within the AOI may also change, possibly affecting the selection of the dry and wet pixels (the number of dry and wet land surfaces may change). Nevertheless, it is nearly impossible to generalize how the land cover type will vary with an increasingly large AOI. Meanwhile, it is also unclear how the temperature and NDVI of the newly included land cover type will vary, as they are affected by the soil/vegetation type, soil moisture content, field irrigation, etc. Increasing the size of the AOI can change the coefficients a and b, thereby influencing H and LE within the original AOI, or make the coefficients, H, and LE invariant. Therefore, we are not able to generalize the effect of the land cover change, although some specific examples are presented in our study. Further studies may statistically investigate the heterogeneities in the global land surface and quantify their effects on the SEBAL-estimated H and LE for other sites.

Acknowledgments

Appendix A. A list of the variables used in this study

Variable	Meaning	Unit
a	Slope of the linear regression between the near-surface air temperature difference and surface temperature	Unitless
b	Intercept of the linear regression between the near-surface air temperature difference and surface temperature	K
C_p	Specific heat of air at constant pressure	J/(m K)
dT_s	Near-surface air temperature difference at $z_1 = 0.1$ m and $z_2 = 2$ m	K
G	Soil heat flux	W/m^2
H	Sensible heat flux	W/m^2
H_{LA} (LE_{LA})	Sensible (latent) heat flux estimated using the large area of interest	W/m^2
H_{SA} (LE_{SA})	Sensible (latent) heat flux estimated using the small area of interest	W/m^2
k	Von Karman's constant	Unitless
L_d	Downward longwave radiation	W/m^2
LE	Latent heat flux	W/m^2
L_u	Upward longwave radiation	W/m^2
r	Surface albedo	Unitless
R_a	Aerodynamic resistance	s/m
R_g	Global solar radiation	W/m^2
R_n	Surface net radiation	W/m^2
T_a	Near-surface air temperature	K
T_{aero}	Aerodynamic temperature	K
T_s	Surface temperature	K
u_{200}	Wind speed at the blending height	m/s
X_{dry}	X variable at the dry pixel ($X = R_n - G, H, LE, T_s, dT_s, R_a$)	
X_{wet}	X variable at the wet pixel ($X = R_n - G, H, LE, T_s, dT_s, R_a$)	
X^H	X variable at the high resolution ($X = a, b, T_s, T_{s,wet}$)	
X^L	X variable at the coarse resolution ($X = a, b, z_{om}, H, LE$)	
δX	Variation of variable X ($X = a, b, dT_s, H_{SA}, T_{s,wet}, T_{s,dry},$ $(R_n - G)_{dry}$)	
$\bar{X}$	Areal averaged X for the $n \times n$ high-resolution pixels ($X = r, \varepsilon_s, T_s, R_a, z_{om}, H, LE, R_n - G$)	
z_{om}	Surface momentum roughness height	m
ψ_m (ψ_h)	Stability correction functions for momentum (heat) transfer	Unitless
ε_a	Atmospheric emissivity	Unitless
ε_s	Surface emissivity	Unitless
ρ	Air density	kg/m^3
σ	Stefan–Boltzmann constant	W/(m^2 K^4)

References

Allen, R.G., Tasumi, M., Trezza, R., 2007. Satellite-based energy balance for mapping evapotranspiration with internalized calibration (METRIC)-model. J. Irrig. Drain. Eng. 133, 380–394.

Anderson, M.C., Norman, J.M., Diak, G.R., Kustas, W.P., Mecikalski, J.R., 1997. A two-source time-integrated model for estimating surface fluxes using thermal infrared remote sensing. Remote Sens. Environ. 60, 195–216.

Baldocchi, D., Falge, E., Gu, L., Olson, R., Hollinger, D., Running, S., Anthoni, P., Bernhofer, C., Davis, K., Evans, R., Fuentes, J., Goldstein, A., Katul, G., Law, B., Lee, X., Malhi, Y., Meyers, T., Munger, W., Oechel, W., Paw, K.T., Pilegaard, K., Schmid, H.P., Valentini, R., Verma, S., Vesala, T., Wilson, K., Wofsy, S., 2001. FLUXNET: a new tool to study the temporal and spatial variability of ecosystem-scale carbon dioxide, water vapor, and energy flux densities. Bull. Am. Meteorol. Soc. 11, 2415–2434.

Bastiaanssen, W.G.M., 1995. Regionalization of surface flux densities and moisture indicators in composite terrain. Ph.D. Thesis, Wageningen Agricultural University, Wageningen, The Netherlands.

Bastiaanssen, W.G.M., Menenti, M., Feddes, R.A., Holtslag, A.A.M., 1998. A remote sensing surface energy balance algorithm for land (SEBAL): 1. Formulation. J. Hydrol. 212–213, 198–212.

Bastiaanssen, W.G.M., Noordman, E.J.M., Pelgrum, H., Davids, G., Thoreson, B.P., Allen, R.G., 2005. SEBAL model with remotely sensed data to improve water-resources management under actual field conditions. J. Irrig. Drain. Eng. 131, 85–93.

Bastiaanssen, W.G.M., Thoreson, B., Clark, B., Davids, G., 2010. Discussion of "application of SEBAL model for mapping evapotranspiration and estimating surface energy fluxes in south-central Nebraska" by Ramesh K. Singh, Ayse Irmak, Suat Irmak, and Derrel L. Martin. J. Irrig. Drain. Eng. 136, 282–283.

Compaoré, H., Hendrickx, J.M.H., Hong, S., Friesen, J., van de Giesen, N.C., Rodgers, C., Szarzynski, J., Vlek, P.L.G., 2008. Evaporation mapping at two scales using optical imagery in the White Volta Basin, Upper East Ghana. Phys. Chem. Earth 33, 127–140.

Gebremichael, M., Wang, J., Sammis, T.W., 2010. Dependence of remote sensing evapotranspiration algorithm on spatial resolution. Atmos. Res. 96, 489–495.

Hong, S., Hendrickx, J.M.H., Borchers, B., 2009. Up-scaling of SEBAL derived evapotranspiration maps from Landsat (30 m) to MODIS (250 m) scale. J. Hydrol. 370, 122–138.

Jiang, L., Islam, S., 1999. A methodology for estimation of surface evapotranspiration over large areas using remote sensing observations. Geophys. Res. Lett. 26, 2773–2776.

Li, Z.-L., Stoll, M.-P., Zhang, R., Jia, L., Su, Z., 2001. On the separate retrieval of soil and vegetation temperatures from ATSR data. Sci. China, Ser. D 44, 97–111.

Li, Z.-L., Zhang, R., Sun, X., Su, H., Tang, X., Zhu, Z.J., Sobrino, A., 2004. Experimental system for the study of the directional thermal emission of natural surfaces. Int. J. Remote Sens. 25, 195–204.

Li, Z.-L., Tang, R., Wan, Z., Bi, Y., Zhou, C., Tang, B., Yan, G., Zhang, X., 2009. A review of current methodologies for regional evapotranspiration estimation from remotely sensed data. Sensors 9, 3801–3853.

Li, Z.-L., Tang, B.-H., Wu, H., Ren, H., Yan, G.J., Wan, Z., Trigo, I.F., Sobrino, J., 2013. Satellite-derived land surface temperature: current status and perspectives. Remote Sens. Environ. 131, 14–37, http://dx.doi.org/10.1016/j.rse.2012.12.008.

Liang, S.L., 2004. Quantitative Remote Sensing of Land Surfaces. John Wiley & Sons, New Jersey.

Long, D., Singh, V.P., Li, Z.-L., 2011. How sensitive is SEBAL to changes in input variables, domain size and satellite sensor? J. Geophys. Res. 116, D21107.

Moran, M.S., Clarke, T.R., Inoue, Y., Vidal, A., 1994. Estimating crop water deficit using the relationship between surface-air temperature and spectral vegetation index. Remote Sens. Environ. 49, 246–363.

Nishida, K., Nemani, R.R., Running, S.W., Glassy, J.M., 2003. An operational remote sensing algorithm of land surface evaporation. J. Geophys. Res. 108, D94270, http://dx.doi.org/10.1029/2002JD002062.

Norman, J.M., Kustas, W.P., Humes, K.S., 1995. A two-source approach for estimating soil and vegetation energy fluxes from observations of directional radiometric surface temperature. Agric. For. Meteorol. 77, 263–293.

Oki, T., Kanae, S., 2006. Global hydrological cycles and world water resources. Science 313, 1068–1072.

Paulson, C.A., 1970. The mathematical representation of wind speed and temperature profiles in the unstable atmospheric surface layer. J. Appl. Meteorol. 9, 857–861.

Price, J.C., 1990. Using spatial context in satellite data to infer regional scale evapotranspiration. IEEE Trans. Geosci. Remote Sens. 28, 940–948.

Roerink, G.J., Su, Z., Menenti, M., 2000. S-SEBI: a simple remote sensing algorithm to estimate the surface energy balance. Phys. Chem. Earth B 25, 147–157.

Singh, R.K., Irmak, A., Irmak, S., Martin, D.L., 2008. Application of SEBAL model for mapping evapotranspiration and estimating surface energy fluxes in south-central Nebraska. J. Irrig. Drain. Eng. 134, 273–285.

Su, Z., 2002. The surface energy balance system (SEBS) for estimation of turbulent heat fluxes. Hydrol. Earth Syst. Sci. 6, 85–99.

Tang, R., Li, Z.-L., Tang, B.H., 2010. An application of the T_s–VI triangle method with enhanced edges determination for evapotranspiration estimation from MODIS data in arid and semi-arid regions: Implementation and validation. Remote Sens. Environ. 114, 540–551.

Tang, R., Li, Z.-L., Jia, Y., Li, C., Sun, X., Kustas, W.P., Anderson, M.C., 2011. An inter-comparison of three remote sensing-based energy balance models using large

aperture scintillometer measurements over a wheat–corn production region. Remote Sens. Environ. 115, 3187–3202.

Tasumi, M., Allen, R.G., Trezza, R., 2008. At-surface reflectance and albedo from satellite for operational calculation of land surface energy balance. J. Hydrol. Eng. 13, 51–63.

Teixeira, A., Bastiaanssen, W.G.M., Ahmad, M.D., Bos, M.G., 2009. Reviewing SEBAL input parameters for assessing evapotranspiration and water productivity for the low-middle São Francisco River basin, Brazil. Part A: calibration and validation. Agric. For. Meteorol. 149, 462–476.

Timmermans, W.J., Kustas, W.P., Anderson, M.C., French, A.N., 2007. An intercomparison of the Surface Energy Balance Algorithm for Land (SEBAL) and the Two-Source Energy Balance (TSEB) modeling schemes. Remote Sens. Environ. 108, 369–384.